



Politecnico
di Bari

Repository Istituzionale dei Prodotti della Ricerca del Politecnico di Bari

Class A prediction of mechanised tunnelling in Rome

This is a post print of the following article

Original Citation:

Class A prediction of mechanised tunnelling in Rome / Losacco, N.; Viggiani, G. M. B.. - In: TUNNELLING AND UNDERGROUND SPACE TECHNOLOGY. - ISSN 0886-7798. - STAMPA. - 87:(2019), pp. 160-173. [10.1016/j.tust.2019.02.020]

Availability:

This version is available at <http://hdl.handle.net/11589/208622> since: 2022-01-31

Published version

DOI:10.1016/j.tust.2019.02.020

Terms of use:

(Article begins on next page)

CLASS A PREDICTION OF MECHANISED TUNNELLING IN ROME

Nunzio LOSACCO*, Giulia M. B. VIGGIANI**

*Università di Roma *Tor Vergata*

**University of Cambridge (formerly Università di Roma *Tor Vergata*)

Corresponding Author:

Nunzio LOSACCO

University of Rome, *Tor Vergata*

Department of Civil Engineering and Computer Science Engineering

Via del Politecnico, 1

00133 – Roma – Italy

Tel. +39.06.72597062

e-mail: nunzio.losacco@uniroma2.it

1 **ABSTRACT**

2 Contract T3 of Line C of Rome underground, currently under construction, crosses the
3 archaeological area of the historical centre, with significant interferences with the existing
4 monumental built environment. A fully instrumented green field control section was
5 established at the beginning of this contract, in representative ground conditions. This
6 paper presents a thorough Class A prediction of the passage of the tunnels through the
7 control section, obtained using a recently developed advanced numerical procedure. The
8 ground was modelled with a non-linear constitutive law, calibrated with all the available
9 data from the geotechnical investigation. The main physical processes occurring around
10 the shield, including cutter-head overcut, shield tapering and tail void grouting were
11 modelled in detail. The numerical results agree qualitatively with the findings from well
12 documented case histories and results from physical models. The installed
13 instrumentation will provide an opportunity to test the ability of the adopted procedure to
14 reproduce quantitatively the measured performance, once the tunnels will cross the
15 control sections and the field data will become available.

16

17 **Key words:**

18 Mechanised tunnelling; Numerical analyses; Class A prediction; Hypoplastic models

1 INTRODUCTION

2 Once completed, Line C of Rome underground will cross the city centre from North-West
3 to South-East and then reach out to the eastern suburbs, for a total length of about 26 km,
4 with 30 stations, and 13 ventilation shafts. The easternmost 9 km of the line are on
5 surface, while the remaining 17 km are bored using two EPB shields. At present,
6 Contracts T4 to T7, comprising the surface stretch, about 10 km of twin running tunnels,
7 and 11 underground stations, have been completed and are in operation. The next stretch
8 of the line, Contract T3, will cross the archaeological area of the historical centre, with
9 significant design challenges connected to presence of buried archaeological remnants
10 and the necessity of minimising the effects of construction on an existing built
11 environment of outstanding historical and monumental value. In fact, the grantor of the
12 project, that is the Municipality of Roma through Roma Metropolitane Ltd, required that
13 the general contractor, Metro C SCpA, set up a multidisciplinary Steering Technical
14 Committee (STC), with the assignments of evaluating the effects of the construction of
15 the line and implementing all necessary procedures to safeguard the monumental
16 heritage.

17 In this framework, a fully instrumented green field control section was established by the
18 STC at the so-called AMA site, in ground conditions representative of those encountered
19 on Contract T3. Fig. 1 is an aerial view of the contract, which runs between San Giovanni
20 and Venezia and comprises about 4 km of twin running tunnels, two stations, and two
21 shafts, indicating the position of the AMA site, at the very beginning of the contract.

22 This work is a Class A prediction of the effects of the passage of Line C running tunnels
23 through the control section by 3D finite element analyses. The term “prediction” is often
24 used when describing the results of numerical or analytical calculations. Boone (2006)

1 recommended that it should always be used in conjunction with a “prediction class” as
2 introduced by Lambe (1973), depending on whether the predictions are made before
3 (Class A), during (Class B), or after (Class C) construction, and, in these last two cases,
4 according to whether or not the results were known (B1 or C1) or not known (B or C) to
5 the authors of the prediction. Most of the so-called predictions are in fact Class C1, so
6 they should be better described as back analyses. Negro (1998) further classified
7 predictions in four categories of increasing thoroughness. In practice, for soft ground
8 tunnelling, the most commonly predicted feature is just the surface settlement trough, but
9 very rarely is the field of subsurface or horizontal displacements predicted or compared
10 with field observations.

11 In recent years, several sophisticated numerical procedures have been proposed to model
12 in great detail mechanised tunnelling, accounting for the main physical processes
13 occurring around the shield. However, these procedures have typically only been tested
14 in idealised conditions, such as uniform soil layers with assumed mechanical behaviour
15 and properties, and, therefore, their ability to reproduce quantitatively rather than
16 qualitatively the actual performance has not been properly assessed.

17 [The main aim of this paper is to test the predictive capability of an advanced numerical](#)
18 [procedure to simulate mechanised tunnelling in a real case.](#) The simulations were carried
19 out before construction, using all the available data from the geotechnical investigation
20 to calibrate the non-linear constitutive laws adopted for the soil; furthermore, all
21 displacement components, both surface and subsurface, as well as excess pore water
22 pressures were predicted. [Once the full set of data from the monitoring system will be](#)
23 [available, comparison with the Class A predictions presented in this paper will provide](#)

1 the validation of the proposed simulation technique, which, in turn will help interpreting
2 the observed behaviour.

3 Unlike other commonly employed approaches, the proposed numerical procedure does
4 not require the introduction of any *a priori* assumptions regarding the expected results
5 (such as volume loss, width of the settlement trough, *etc.*) as it aims at reproducing
6 realistically the perturbation induced in the ground by the TBM operation. Hence, the
7 technique could be used with confidence to study soil-structure simulation problems,
8 which usually are the most relevant application, without any significant adaptation of the
9 method.

11 **1 BACKGROUND**

12 Numerical analyses of mechanised tunnel excavation are often carried out using
13 simplified approaches in which fictitious perturbations are applied at the excavation
14 boundary, thus disregarding the physical processes occurring around the shield. These
15 perturbations may consist of either applied stress distributions (e.g. Mroueh and
16 Shahrour, 2008), or prescribed displacement fields (e.g. Rampello et al., 2012; Losacco
17 et al., 2014, 2016; Boldini et al., 2018), generally calibrated by trial and error to obtain a
18 given value of volume loss V_L and a realistic shape of the settlement trough at ground
19 surface in greenfield conditions. Hence, both V_L and the trough width parameter K are
20 input data, and there is a certain degree of arbitrariness in their choice.

21 Recently, more sophisticated numerical strategies have been proposed, simulating some
22 of the physical processes occurring during mechanised tunnelling, including application
23 of a face support pressure, interaction between the shield and the surrounding soil, lining
24 installation and backfill grouting of the tail void.

1 Simulation of the face pressure through a force distribution on the tunnel face, either
2 uniform (e.g. Founta et al. 2013, Chakeri et al. 2013) or linearly increasing with depth
3 (e.g. Dias and Kastner, 2013; Kavvadas et al., 2017) is by far the most common choice.
4 Simulation of ground loss along the steering gap has been carried out using a wide variety
5 of approaches: either by prescribing volumetric strains (e.g. Broere and Brinkgreve,
6 2002) or radial displacements (e.g. Dias and Kastner, 2013; Founta et al., 2013) to the
7 shield elements or by applying a purposely calibrated stress field at the excavation
8 boundary (Castellanza et al., 2013) or by introducing fictitious solid elements with
9 adequately chosen stiffness (Lambrughi et al., 2012). In all those cases, the convergence
10 due to the gap is an imposed condition rather than a result of the analysis. [Some authors](#)
11 [allow the tunnel boundary to deform until the limit imposed by the actual shield geometry,](#)
12 [that is not explicitly modelled \(Jenck and Dias, 2004; Do et al., 2013a; Comodromos et](#)
13 [al., 2014\).](#) In other studies, the shield was modelled using a separate, independent mesh
14 and the interaction with the surrounding soil was enforced using contact laws (e.g. Kasper
15 and Meschke, 2004; Meschke et al., 2011).

16 Grouting of the tail void is often simulated through a radial pressure distribution applied
17 at the tunnel boundary (Dias and Kastner, 2013; Do et al., 2013a). The layer of hardened
18 grout is modelled using solid elements in Migliazza et al. (2009) and Chakeri et al. (2013).
19 Progressive hardening can be simulated using time-dependent elastic properties for the
20 elements of the backfill layer (e.g. Meschke et al., 2011; Lambrughi et al., 2012;
21 [Comodromos et al., 2014\).](#)

22 [Some recent studies \(Comodromos et al., 2014; Ochmański et al., 2018\) showed the](#)
23 [successful performance of such detailed models of mechanized tunnelling both in](#)

1 greenfield conditions in matching the observed soil response, although in class C
2 predictions which considered limited sets of field data.

3 This study adopts a slightly modified version of the simulation technique recently
4 proposed by Kavvadas et al. (2017), which focuses on modelling in detail the steering
5 gap and the tail void grouting, assumed to be the most significant factors influencing the
6 ground loss. In this approach, no arbitrary perturbations are applied at the tunnel boundary
7 nor is any calibration of fictitious material properties involved.

8 9 **2 THE SITE**

10 A geological section of the area, transverse to the tunnel axes, is shown in Fig. 2. The soil
11 profile is based on the boreholes cored in five campaigns of geotechnical investigation
12 and more recently for the installation of the instruments in the monitoring section at the
13 AMA site. Starting from the almost horizontal ground surface, the soil profile comprises
14 the following sub-horizontal layers:

15 1) made ground (R): very heterogeneous gravelly and sandy soils in a pyroclastic matrix,
16 17-18 m thick;

17 2) recent alluvial deposits of the Tiber river (LSO): sandy silts and organic silty sands,
18 with a thickness decreasing from of about 8 m in the northern part of the site, to disappear
19 south of the tunnels;

20 3) Pleistocene alluvial deposits of Paleotevere (St/Ar): silty sands and sandy silts (St) and
21 clayey silts (Ar), with a maximum thickness of 12 m and a ditch filled with the overlying
22 LSO soil north of the tunnels;

23 4) Pleistocene fluvial deposit (SG): sands and gravels, with an approximately constant
24 thickness of 10 m;

1 5) Monte Vaticano clay (Apl): over-consolidated and very stiff silty clays and clayey silts,
2 with an almost horizontal roof at 5.5 m a.s.l. and extending to a depth of hundreds of
3 meters.

4 The ground water table is located at a depth of about 9.0 m; piezometer measurements
5 indicate a downward seepage occurring through the alluvial deposits, with a hydraulic
6 head in the SG layer about 9.0 m lower than in the made ground.

7 Fig. 3 summarises the main physical properties of the soil layers at the site.

8 A simplified geotechnical model with horizontal layers and ground surface was assumed
9 as follows, in which, due to their similar mechanical properties, LSO and St/Ar were
10 considered as a single layer (LSO in the following):

11 1) R, from ground surface to 17 m depth;

12 2) LSO, from 17 m to 30 m depth;

13 3) SG, from 30 m to 42 m depth;

14 4) Apl, from 42 m to indefinite depth.

15 The AMA site is located at the beginning of contract T3, between Amba Aradam/Ipponio
16 Station and multi-functional Shaft 3.3, approximately 300 m east of the station. The two
17 tunnels will be excavated in sequence, from Shaft 3.3 towards Amba Aradam/Ipponio
18 Station; the excavation of the South Tunnel will start about 60 days after the North
19 Tunnel, with a longitudinal distance of approximately 120 m between the two excavation
20 faces. The tunnel axes run approximately 14.5 m apart at a depth z_0 of about 25 m below
21 ground level.

22 Figs. 4 (a) and (b) show a plan view of the site and a cross section with the subsurface
23 instrumentation, respectively. The latter comprises 7 Trivecs, for the measurement of all

1 components of displacement, 5 inclinometers, and 5 vibrating wire piezometers. Surface
2 levelling points are also installed in the section.

3

4 **3 DETAILS OF NUMERICAL MODEL**

5 **3.1 Simulation of tunnel excavation**

6 The analyses were carried out using the finite element software Abaqus 6.14, adopting
7 the technique described in Kavvadas et al. (2017) and recently employed by Litsas et al.
8 (2018) to simulate the tunnelling process. The proposed technique accounts for the main
9 physical processes—taking place at the excavation boundary, which are shown
10 schematically in Fig. 5.

11 The two EPB shields used for the excavation are identical, with total length of 11.8 m and
12 maximum diameter of the cutting wheel $D = 6.71$ m. The diameter of the shield decreases
13 from 6.69 m behind the cutterhead to 6.67 m at the tail, resulting in an annular gap
14 increasing from 10 mm to 20 mm towards the shield tail. The outer diameter of the lining
15 is 6.40 m, resulting in a tail void gap of 155 mm. The shields are modelled as rigid bodies
16 and their rotation is constantly constrained; the self-weight, including the weight of the
17 machinery enclosed in the shield and of the muck in the excavation chamber, is applied
18 as a concentrated vertical load.

19 A contact law is activated at all stages to simulate interaction between the shield and the
20 soil around the excavation boundary: a pressure-overclosure relation with very large
21 stiffness is adopted for contact in the normal direction, while frictionless contact is
22 assumed in the tangential direction. The contact constraints are enforced using a penalty
23 method that minimises overclosure and improves the convergence of the FE solver.

1 At each excavation stage the shield is advanced a distance $L_{exc} = 2.8$ m, i.e. the length of
2 two lining rings, then elements representing the lining are activated right behind the tail
3 over the same length L_{exc} ; the front nodes of the newly activated lining elements are fixed,
4 assuming that their movements are constrained by the action of the hydraulic jacks, that
5 are not explicitly simulated. The lining is modelled as monolithic, without any joints
6 between adjacent rings or segments, as previous studies (Do et al., 2013b, 2013c) have
7 demonstrated that taking into account its segmental nature does not affect significantly
8 predicted ground displacements. Prediction of structural forces in the lining is out of the
9 scope of this paper.

10 Pressurised backfill injections will be performed during the excavation phase using a two-
11 component grout. In the numerical model, this is simulated through the application of a
12 uniformly distributed pressure p_{grout} over the length L_{exc} immediately behind the shield
13 tail, acting both on the excavation boundary and on the extrados of the freshly activated
14 lining ring, assuming that right after the injection the grout is in a liquid state. Starting
15 from a distance L_{exc} behind the shield tail, hardening of the grout is simulated by removing
16 the radial pressure and activating a ring of solid elements with initial isotropic stress equal
17 to p_{grout} and with Young's modulus increasing with time. The grout injection pressure was
18 fixed to $p_{grout} = 250$ kPa, that is the average between the design value of 400 kPa targeted
19 by the general contractor and the minimum alarm threshold of 100 kPa. Some preliminary
20 analyses, presented below, were undertaken to assess the effect of a variation of p_{grout}
21 within this range.

22 Consistently with the indications of the general contractor, a support pressure equal to the
23 *in situ* horizontal total stress is applied at the excavation face at all stages, assuming

1 optimal operation of the EPB shield so that little or no ground loss is induced at the tunnel
2 face.

3 Given the design tunnelling rate of 10 m/day in the examined area, carried out on a
4 6 days/week basis, a corresponding average advancement rate was assumed such that
5 each L_{exc} long excavation step was carried out in 8 hours.

6

7 **3.2 FE model**

8 Fig. 6 shows the Finite Element models employed for the analyses. The bottom boundary
9 of the mesh corresponds to the roof of the stiff clay deposit, i.e. 42 m below ground
10 surface.

11 The finite element mesh extends 154.5 m in the x direction, transversal to the tunnel axis,
12 and 170.0 m in the longitudinal y direction. Its size is sufficiently large to minimise the
13 effect of the boundaries; the maximum excavation length from the initial boundary is
14 $L_{max} = 120.4$ m. The monitoring section is at $y_{mon} = 61.6$ m from the initial boundary,
15 approximately half way along the tunnel extent at the end of the analysis. The mesh
16 contains 62719 nodes and 56496 hexahedral 8-noded elements; this density was chosen
17 after a preliminary set of analyses to compromise between solution accuracy and
18 reasonable calculation times.

19 The displacements of the nodes on the side faces of the model are constrained in the
20 normal direction, while all components of displacements are constrained at the base.

21 Constant pore pressure is prescribed at the interface between the R and the LSO layers
22 and between the latter and the SG layers, so as to reproduce the observed downward
23 stationary seepage at the beginning of the analysis; a no flow condition is always enforced
24 at the tunnel boundary.

1 All the analyses were conducted in terms of effective stress and employing a coupled
2 consolidation scheme. The whole simulation can be subdivided into four main stages as
3 follows:

4 1. Geostatic equilibrium: application of the initial effective stress field and distribution
5 of pore water pressure, in equilibrium with gravity load and hydraulic boundary
6 conditions;

7 2. North Tunnel excavation: excavation of North Tunnel up to $L_{\max} = 120.4$ m from initial
8 boundary, with an average excavation rate of 0.35 m/hour.

9 3. Consolidation: consolidation analysis for a duration corresponding to the time gap
10 between the passages of the two TBMs;

11 4. South Tunnel excavation: same as for North Tunnel.

12

13 **3.3 Constitutive models for soils and structural materials**

14 Hypoplastic models for granular materials (von Wolffersdorff, 1996) and for clays
15 (Mašín, 2005) were used for layers R and LSO, respectively. These models are able to
16 reproduce the main relevant features of soil response, including non-linearity of stress-
17 strain behaviour, dependency of stiffness and strength on mean effective stress and void
18 ratio, evolving dilatancy, and critical state conditions. The introduction of the Inter
19 Granular Strain concept (Niemunis and Herle, 1997) into the original version of the
20 models permits to take into account initial large stiffness at small strain, decay of stiffness
21 with shear strain, and influence of recent strain history.

22 The model for granular materials requires eight material parameters, namely: the critical
23 state friction angle φ_{cs} ; the reference stress h_s and the exponent n , controlling the overall
24 slope and curvature of asymptotic normal compression paths in $e:p'$ plane; the minimum,

1 critical state and maximum voids ratio at zero mean effective stress, e_{d0} , e_{c0} and e_{i0} ; two
2 exponents α and β , which rule the dependency of the angle of friction at peak on void
3 ratio and the stiffness in shearing, respectively.

4 The clay hypoplastic model requires five material parameters, similar to those of
5 Modified Cam Clay (Roscoe and Burland, 1968): φ_{cs} is the critical state friction angle, N
6 and λ^* control the position of the isotropic normal compression line and κ^* the slope of
7 the isotropic unloading line in a $\log(1+e):\log p$ plane, while the ratio λ^*/κ^* dictates the
8 shape of the state boundary surface. Finally, parameter ν controls the shear stiffness.

9 The introduction of the intergranular strain requires calibration of 5 or 6 additional
10 parameters, depending on the model: the shear stiffness at very small strain,
11 corresponding to 180° strain path reversal, is controlled by parameter m_R in the model for
12 sand, and by parameters A_g and n_g in the clay model; m_T and m_{rat} control the initial shear
13 modulus on a 90° change of direction of the strain path in the sand and clay models,
14 respectively; R defines the size of the pseudo-elastic range in the strain space; β_r and χ
15 control the rate of degradation of stiffness with strain.

16 As no laboratory tests were available for the coarse-grained made ground, the critical
17 state friction angle φ_{cs} was obtained from the results of SPT and CPT tests and the
18 intergranular strain parameter m_R by fitting the profile of G_0 with depth from cross-hole
19 tests. For the remaining material constants, average values were assumed based on those
20 provided in Herle and Gudheus (1999) for six different sandy soils.

21 Parameters A_g and n_g of the clay model were obtained from the profile of G_0 with depth;
22 R , β and χ were calibrated based on the results of resonant column tests, while a typical
23 value for m_{rat} was taken from the literature. Fig. 7 shows the results of the calibration of
24 N , λ^* and κ^* for the LSO layer, using data from oedometer tests. Finally, the value of ν

1 was obtained by fitting the results of isotropically consolidated drained and undrained
2 triaxial compression tests, and K_0 -consolidated-undrained triaxial extension tests, as
3 shown in Figs. 8(a) to (d). The constitutive model reproduces the observed soil behaviour
4 remarkably well under a variety of different test conditions.

5 To account for the stress history, either the void ratio, e , or the overconsolidation ratio,
6 OCR , can be used as a state variable in the two hypoplastic models, and their initial values
7 must be prescribed at the beginning of the analyses. A constant void ratio $e = 1.0$ was
8 assumed for the R layer, whereas a constant $OCR = 1.3$ was used for the LSO layer.

9 The SG layer was modelled as linear elastic-perfectly plastic, with a constant elastic shear
10 modulus equal to one third of the mean value of the data from cross-hole tests, to account
11 for the expected shear strain level, while the angle of friction was derived from the SPT
12 tests.

13 Tables 1-3 summarise the assumed values of material constants for the three soil layers,
14 together with their unit weight, γ , coefficient of earth pressure at rest, K_0 , and permeability
15 k . The coefficient of permeability, k , was obtained from Lefranc tests while K_0 was
16 estimated as (Mayne and Kulhawy, 1982):

$$17 \quad K_0 = (1 - \sin \varphi)OCR^{\sin \varphi} \quad (1)$$

18 assuming $OCR = 1.0$ for both R and SG layers.

19 In the hardening phase, the tail void grout is modelled as linear elastic, with time
20 dependent Young's modulus $E_1 = 0.5$ GPa after one day and $E_{28} = 1$ GPa after 28 days
21 (Kasper and Meschke, 2004). It is assumed that the grout behaves as an incompressible
22 fluid, with Poisson's ratio close to 0.5, until a time of 5 hours from the injection, and then
23 its value is ramped down to 0.2 linearly with time.

1 The lining is isotropic linear elastic, with Young's modulus $E = 31$ GPa Poisson's ratio
2 $\nu = 0.2$.

3

4 **4 PRELIMINARY ANALYSES**

5 The volume loss caused by the sole full closure of the tail void would be about 9%, with
6 potentially severe adverse effects due to late or ineffective grouting. Field observations
7 in recent tunnelling projects, (e.g., Gens et al. 2011, Fagnoli et al. 2013) show that the
8 tail void might be the largest source of volume loss due to the operation of an EPB shield.
9 A sensitivity analysis was therefore carried out to assess the influence of grouting
10 pressure on the displacements induced by the excavation.

11 In these preliminary analyses the excavation of the North Tunnel only was simulated,
12 hence half of the problem was modelled, taking advantage of symmetry. Three values of
13 tail void grout pressure were used, namely 400 kPa (maximum design value), 250 kPa
14 (reference value), and 100 kPa (minimum design alarm threshold), as per indications of
15 the general contractor.

16 Figs. 9 (a,b) report the effects of the grout pressure on the tunnel boundary, for three
17 nodes located at the tunnel crown, invert and springline. As shown in Fig. 9(a), when the
18 reference value of 250 kPa is applied, a recovery of displacements as high as 4.5 mm is
19 recorded at the springline, i.e. almost 25% of the convergence occurred during the passage
20 of the shield, while the radial displacements at the invert remain constant after grout
21 injection. When the maximum value of grouting pressure is employed, the recovery at the
22 springline rises to 57% and a backward radial movement is predicted at the tunnel invert.
23 On the contrary, when the minimum pressure is applied, the convergence at the invert

1 rises by almost 50%, and a slight increase of convergence is predicted at the crown, while
2 it remains approximately constant at the springline.

3 Fig. 9(b) shows that, at all locations, small positive excess pore pressures develop during
4 the shield advance through the control section, reaching a peak right after the passage of
5 the tail, due to injection of grout into the tail gap at 250 kPa and 400 kPa. The relative
6 amplitude of this peak, with respect to the steady-state value of pore pressure, is largest
7 at the springline, where the radial in situ stress is the lowest, and very small at the invert,
8 where the initial radial stress is the highest. At all locations the excess pressure is
9 dissipated after approximately further 10 m advance of the shield, i.e. about 1 day,
10 suggesting that, in this case, excavation is mainly a drained process, due to the low
11 advancement rate and the relatively large permeability of the LSO layer. The relatively
12 modest change of pore pressure from the initial to the final steady-state, is consistent with
13 the distortion of the flow net due to the introduction of the tunnel boundary, assumed
14 impervious, into the pre-existing downwards seepage flow.

15 The surface settlement troughs at the end of the analysis, both in the longitudinal direction
16 and in the transverse monitoring section are plotted in Figs. 10(a) and (b) respectively.

17 The effect of increasing the grout pressures from the reference to the maximum value,
18 although significant close to the tunnel, is minimal in terms of settlements at ground
19 surface. On the other hand, an appreciable increase in surface settlements is computed for
20 the lowest grout pressure, with a relative difference of approximately 17.5 %. The volume
21 loss calculated from the surface transverse settlement trough is 0.30% for the reference
22 case with $p_{\text{grout}} = 250$ kPa, while $V_L = 0.28\%$ and 0.38% are obtained for $p_{\text{grout}} = 400$ kPa
23 and 100 kPa respectively (relative variation of -7% and 27%). These values of volume

1 loss are in the range expected for similar ground conditions and tunnelling techniques
2 (Bilotta et al., 2002; Fagnoli et al., 2015b, 2015a; Mair and Taylor, 1999).

3 The results described in this section suggest that if complete filling of the tail void is
4 carried out immediately during the shield advance, in such a way to stop or even reduce
5 the settlement at the tunnel crown, the settlement of the ground surface can be controlled
6 effectively, and that the effect of increasing the grouting pressure, although significant at
7 the tunnel boundary, is fairly limited close to the ground surface. This is consistent with
8 field observations.

9

10 **5 CLASS A PREDICTIONS**

11 Figs. 11(a) and (b) show the evolution of the surface longitudinal settlement troughs due
12 to the excavation of the two tunnels above their respective centrelines; the displacements
13 shown for the South Tunnel are the increments relative to those induced by the first
14 excavation. For each curve, the arrows indicate the position y of the tunnel face. The
15 construction of the North Tunnel induces a maximum settlement $w_{\max} = 3.47$ mm, with a
16 settlement at the tunnel face equal to 40% w_{\max} ; a well-defined steady-state zone can be
17 observed starting from approximately 40 m behind the excavation face. The excavation
18 of the South tunnel causes $w_{\max} = 5.91$ mm above its centreline, i.e. 70% larger than the
19 value calculated for the previous excavation, with 33% w_{\max} at the tunnel face. Such a
20 large increase of final settlement is due to the disturbance induced by the construction of
21 the previous tunnel, given the relatively small distance $s = 2.16 D$ between the two axes.
22 The same behaviour was observed by Wan et al. (2017) for the construction of the twin
23 tunnels of the Crossrail project with similar values of z_0/D and s/D , in terms of both
24 relative increase of maximum settlement and relative settlement above the tunnel face.

1 Fig. 12 shows the computed transverse settlement troughs for three depths, $z = 0.0, 9.0$
2 and 17.0 m, and compares them with those obtained from the well-known Gaussian
3 empirical relationships (Peck, 1969). The relative difference between the maximum
4 settlements produced by excavation of the two tunnels decreases with depth. A notable
5 feature, confirmed by field observations in many case histories (e.g. Fagnoli et al., 2015a;
6 Wan et al., 2017), is the asymmetry of the settlement trough induced by the second
7 excavation, with the northern half being systematically wider than the other; once again,
8 this is ascribed to the disturbance induced by the excavation of the North Tunnel. As in
9 Wan et al. (2017), the best-fit curves were obtained by fitting the settlement troughs for
10 points with $w/w_{\max} \geq 0.36$, fixing the value of w_{\max} and the corresponding abscissa that,
11 for the South Tunnel, does not coincide with the centreline, as observed also by Chen et
12 al. (2011). Furthermore, a different fit was performed for the two halves of the South
13 Tunnel settlement trough. A varying trough width parameter K with depth was assumed,
14 as proposed by Moh et al. (1996):

$$15 \quad K = K_{(z=0)} \left(\frac{z_0 - z}{z_0} \right)^{m-1} \quad (2)$$

16 with $m = 0.4$, which is the suggested value for silty sands.

17 Figs. 13(a) and (b) show the vectors of incremental displacements for the first and the
18 second excavation; at any depth, the focus of incremental displacement vectors is deeper
19 for the South Tunnel than for the North Tunnel, and it is shifted towards the latter close
20 to the ground surface while it tends to move away from it at greater depths. Also, the zone
21 of influence for the second excavation is wider than that for the first excavation.

22 Fig. 14(a) shows the computed variation of the depth of the focus of incremental
23 displacements z_f with depth for the two excavations; the horizontal offset x_f with respect

1 to the centreline is also plotted for the South Tunnel (negative towards North).
2 Consistently with results from field observations (Chen et al., 2011; Wan et al., 2017) and
3 numerical (Viggiani and Soccodato, 2004) and physical (Grant and Taylor, 2000)
4 modelling, z_f/z_0 increases linearly with z/z_0 , with the foci being located below the tunnel
5 axis for $z > 0.15 z_0$, approximately. For the South Tunnel, the offset x_f decreases more
6 than linearly with depth. It is worth noting that the asymmetry of the soil response to the
7 excavation of the South Tunnel, due to the disturbance induced by the former bore, causes
8 the foci of displacement vectors at depth to be poorly defined. Hence, for points located
9 at depth, the coordinates of the focus must be regarded as the centre of a blurred area.

10 Fig. 14(b) shows the transverse profiles of horizontal displacements for the same depths
11 as in Fig. 12 and compares them with the empirical prediction obtained using the
12 increasing depth and varying offset of the focus of incremental displacements given in
13 Fig. 13(a). As for the transverse settlement trough, the distribution of horizontal
14 displacements induced by the South Tunnel is asymmetric, with the point of null
15 horizontal displacement at ground surface shifted towards the North Tunnel, consistently
16 with the position of the maximum settlement. However, at larger depth, this point tends
17 to move back towards the centreline of the South Tunnel. The corrected empirical
18 relations are generally in very good agreement with the numerical results, although for
19 the South Tunnel, the match degrades with depth, consistently with the more dispersed
20 directions of displacement vectors.

21 The profiles of K and V_L with depth are plotted in Figs. 15(a) and (b). As mentioned
22 above, the northern half of the transverse settlement trough induced by the second tunnel
23 is larger than the southern half at all depths. Consistently, the volume loss corresponding

1 to the northern half is also larger. Both the relationship proposed by Mair and Taylor
2 (1999):

$$3 \quad K = \left[0.175 \left(\frac{z_0}{z_0 - z} \right) + 0.325 \right] \quad (3)$$

4 and Moh et al. (1996) (see Eq. (2) above) match the predicted variation of K with depth
5 in the R layer reasonably well. The volume loss does not change significantly over the
6 thickness of the made ground layer, implying small dilatancy connected to the low strain
7 levels, whereas a sharp increase of V_L is recorded below the contact between the made
8 ground and the LSO layer.

9 Figs. 16 and 17 report the profiles of settlements and transverse horizontal displacements
10 predicted at the location of the Trivecs in the monitoring section. Excavation of the North
11 Tunnel, Fig. 16(a), induces minimal tensile strains in the R layer; a sudden increase of
12 settlements, with significant tensile strains, is predicted in the LSO layer right above the
13 tunnel crown. Some compressive strain is obtained close to the tunnel springline (TR6
14 and TR4), as expected.

15 The pattern of vertical displacements due to excavation of the South Tunnel, given in Fig.
16 16(b), is very similar to that for the first tunnel, although larger values of absolute
17 settlements are obtained. In both cases, steady-state conditions are achieved before the
18 excavation face is 3 diameters (i.e. about 20 m) ahead of the monitoring section.

19 The predicted greenfield profiles of horizontal displacements are clearly affected by tail
20 grouting. The soil close to the springline tends to displace towards the tunnel axis as the
21 excavation face approaches the monitoring section and is pushed backwards after the
22 passage of the shield tail, as shown for the North Tunnel at TR6 and TR4 in Fig. 17(a).

23 The same behaviour is predicted at TR4 and TR2 for the excavation of the South tunnel

1 in Fig. 17(b); again, the results confirm the asymmetry of the horizontal displacement
2 field induced by the second excavation.

3 The contours of volumetric strain displayed in Figs. 18 (a) and (b) highlight an area of
4 significant expansion around the tunnels (maximum 0.75%), corresponding
5 approximately to the thickness of the LSO layer. While the induced soil dilation does not
6 change between the two excavations, Fig. 18 (b) shows a remarkable increase of
7 compressive strains for the second excavation: close to the surface, above the centreline,
8 and at the springline of the South Tunnel, in particular near the North Tunnel.

9 Figs. 19(a) and (b) suggest that the predicted volumetric expansion is associated with
10 intense shearing in the vicinity of the tunnels and that, again, the strain regime is generally
11 enhanced during the passage of the second tunnel.

12 Finally, Figs. 20 (a) and (b) report the predicted pore water pressures at the locations of
13 the five installed piezometers. As before, the permanent variation of pore water pressure
14 is small and can be ascribed exclusively to the change of hydraulic boundary conditions
15 in the calculation domain, following activation of the impervious boundary of the tunnels
16 into the pre-existing downward seepage flow.

17

18 **6 SUMMARY AND CONCLUSIONS**

19 A numerical “Class A” prediction of the passage of the running tunnels of Line C of Roma
20 underground through a fully instrumented greenfield control section was carried out. Care
21 was taken to predict displacements and excess pore water pressures at the same locations
22 where instrumentation is installed on site, in order to permit direct comparison with the
23 real field data, which will become available when the tunnels will cross the instrumented
24 sections.

1 A recently proposed advanced numerical procedure was adopted, considering the main
2 features of the shield and the main physical processes taking place during mechanised
3 tunnelling. The volume loss and the trough width parameter are results of the analyses.
4 The mechanical behaviour of all soils was simulated using hypoplastic models able to
5 reproduce the main relevant features of the mechanical response, including non-linearity
6 of stress-strain behaviour, dependency of stiffness and strength on mean effective stress
7 and void ratio, evolving dilatancy, and critical state conditions. These were carefully
8 calibrated using all the available data from laboratory and site tests.

9 The main findings of this predictive exercise can be summarised as follows:

- 10 - tail void grouting can control very effectively ground surface settlements; the effect of
11 increasing or decreasing the grouting pressure, although significant at the tunnel
12 boundary, is fairly limited close to the ground surface;
- 13 - excess pore water pressures generated by the tunnelling dissipate rapidly, suggesting
14 that, for the case under examination, due to the low advancement rate and the relatively
15 large permeability of the soil, the process is essentially drained. Permanent changes in
16 pore water pressures after the passage of the shield are due to the change of hydraulic
17 boundary conditions along the impervious boundary of the tunnels;
- 18 - the settlement trough induced by excavation of the second tunnel is **significantly larger**
19 **than the first and also** not symmetric, with the abscissa of maximum settlement shifted
20 towards the first tunnel, and the corresponding half of the settlement trough
21 systematically wider than the other;
- 22 - the distribution of horizontal displacements induced by the second tunnel is also
23 asymmetric, with the point of null horizontal displacement at ground surface shifted
24 towards the first tunnel, consistently with the position of the maximum settlement;

1 - volume loss is essentially constant in the made ground layer, due to the low strain
2 levels. A sharp increase of volume loss is predicted below the contact between the
3 made ground and the silty clay layer, close to the tunnel crown, where relatively large
4 shear strains concentrate.

5 Although the numerical results are promising, being in qualitative and in some instances
6 quantitative agreement with the findings from well documented case histories and results
7 of physical models, the final validation of the proposed analyses will be provided by
8 comparison with the real field data, once the tunnels will cross the control section.

9 The proposed simulation approach requires quite a complex modelling phase and implies
10 long calculation times, due to the large number of degrees of freedom, the need to
11 simulate the progressive advance of the excavation, the many sources of non-linearity
12 (hypoplastic constitutive models, soil-shield contact interaction, coupled consolidation).
13 Hence, it is not likely to be adopted as a routine tool in tunnel design but can be extremely
14 valuable to assess the expected effects of tunnel excavations (volume loss, displacement
15 field at depth, etc.) for the calibration of simpler models or it can be used for the analysis
16 of critical cases, such as when the potential damage on a sensitive structure must be
17 estimated.

18

19 **ACKNOWLEDGMENTS**

20 The work described in this paper was carried out with the financial support of the
21 European Commission through Large Collaborative Project: NeTTUN “New
22 Technologies for Tunnelling and UNDERground Works”, Grant Agreement Number
23 280712. The Authors are indebted to Metro C ScPA, particularly to Mr. Eliano Romani,
24 Mr. Ivan Mammone and Ms. Grazia Di Mucci, for making available all the results from

1 the geotechnical investigation and more generally for providing constant support
2 throughout the project and to Mr. Giorgio Pezzetti of SMAK Sas. The analyses require
3 significant computational resources and were carried out on the Tier-1 HPC system
4 Galileo at CINECA, under ISCRA Class C project TEREsa “Tunnel Excavation Reliable
5 Simulation Approach”.

6

7 REFERENCES

- 8 Bilotta, E., Russo, G., Viggiani, C., 2002. Cedimenti indotti da gallerie superficiali in
9 ambiente urbano. XXI Convegno Naz. Geotec. Opere Geotec. Ambiente Urbano.
- 10 Boldini, D., Losacco, N., Bertolin, S., Amorosi, A., 2018. Finite Element modelling of
11 tunnelling-induced displacements on framed structures. *Tunn. Undergr. Space*
12 *Technol.* 80, 222–231. <https://doi.org/10.1016/j.tust.2018.06.019>
- 13 Boone, S.J., 2006. Deep Excavations: General Report, in: Bakker et al. (Ed.),
14 Geotechnical Aspects of Underground Construction in Soft Ground. Taylor &
15 Francis, London, pp. 81–90.
- 16 Broere, W., Brinkgreve, R., 2002. Phased simulation of a tunnel boring process in soft
17 soil. *Numer. Methods Geotech. Eng.*
- 18 Castellanza, R., Betti, D., Mancinelli, L., Morerio, C., Tedesco, S., Bueno, V., 2013. 3D
19 Numerical Prediction for TBM-EPB Excavations under Railways Bridges in
20 Milan (Italy), in: *Proceeding of the 3rd International Conference on*
21 *Computational Methods in Tunnelling*, (Euro:Tun 2013). pp. 119–130.
- 22 Chakeri, H., Ozcelik, Y., Unver, B., 2013. Effects of important factors on surface
23 settlement prediction for metro tunnel excavated by EPB. *Tunn. Undergr. Space*
24 *Technol.* 36, 14–23. <https://doi.org/10.1016/j.tust.2013.02.002>
- 25 Chen, R.P., Zhu, J., Liu, W., Tang, X.W., 2011. Ground movement induced by parallel
26 EPB tunnels in silty soils. *Tunn. Undergr. Space Technol.* 26, 163–171.
27 <https://doi.org/10.1016/j.tust.2010.09.004>
- 28 Comodromos, E., Papadopoulou, M., Konstantinidis, G., 2014. Numerical Assessment of
29 Subsidence and Adjacent Building Movements Induced by TBM-EPB Tunneling.
30 *J. Geotech. Geoenvironmental Eng.* 140, 4014061.
31 [https://doi.org/10.1061/\(ASCE\)GT.1943-5606.0001166](https://doi.org/10.1061/(ASCE)GT.1943-5606.0001166)
- 32 Dias, D., Kastner, R., 2013. Movements caused by the excavation of tunnels using face
33 pressurized shields — Analysis of monitoring and numerical modeling results.
34 *Eng. Geol.* 152, 17–25. <https://doi.org/10.1016/j.enggeo.2012.10.002>
- 35 Do, N.-A., Dias, D., Oreste, P., Djeran-Maigre, I., 2013a. 3D modelling for mechanized
36 tunnelling in soft ground-influence of the constitutive model. *Am. J. Appl. Sci.*
37 10, 863.
- 38 Do, N.-A., Dias, D., Oreste, P., Djeran-Maigre, I., 2013b. Three-dimensional numerical
39 simulation for mechanized tunnelling in soft ground: the influence of the joint
40 pattern. *Acta Geotech.* 1–22. <https://doi.org/10.1007/s11440-013-0279-7>

- 1 Do, N.-A., Dias, D., Oreste, P., Djeran-Maigre, I., 2013c. 2D numerical investigation of
2 segmental tunnel lining behavior. *Tunn. Undergr. Space Technol.* 37, 115–127.
3 <https://doi.org/10.1016/j.tust.2013.03.008>
- 4 Fargnoli, V., Boldini, D., Amorosi, A., 2015a. Twin tunnel excavation in coarse grained
5 soils: Observations and numerical back-predictions under free field conditions
6 and in presence of a surface structure. *Tunn. Undergr. Space Technol.* 49, 454–
7 469. <https://doi.org/10.1016/j.tust.2015.06.003>
- 8 Fargnoli, V., Boldini, D., Amorosi, A., 2013. TBM tunnelling-induced settlements in
9 coarse-grained soils: The case of the new Milan underground line 5. *Tunn.*
10 *Undergr. Space Technol.* 38, 336–347. <https://doi.org/10.1016/j.tust.2013.07.015>
- 11 Fargnoli, V., Gragnano, C.G., Boldini, D., Amorosi, A., 2015b. 3D numerical modelling
12 of soil–structure interaction during EPB tunnelling. *Géotechnique* 65, 23–37.
13 <https://doi.org/10.1680/geot.14.P.091>
- 14 Founta, V., Ninic, J., Whittle, A.J., Meschke, G., Stascheit, J., 2013. Numerical
15 Simulation of Ground Movements Due To EPB Tunnelling in Clay, in:
16 Proceeding of the 3rd International Conference on Computational Methods in
17 Tunnelling, (Euro:Tun 2013). pp. 97–108.
- 18 Gens, A., Di Mariano, A., Yubero, M., 2011. EPB tunneling in deltaic deposits:
19 observations of ground movements, in: 7th International Symposium
20 Geotechnical Aspects of Underground Construction in Soft Ground.
- 21 Grant, R.J., Taylor, R.N., 2000. Tunnelling-induced ground movements in clay. *Proc Inst.*
22 *Civ. Eng.-Geotech. Eng.* 143, 43–55.
- 23 Herle, I., Gudehus, G., 1999. Determination of parameters of a hypoplastic constitutive
24 model from properties of grain assemblies. *Mech. Cohesive-Frict. Mater.* 4, 461–
25 486.
- 26 Jenck, O., Dias, D., 2004. Analyse tridimensionnelle en différences finies de l’interaction
27 entre une structure en béton et le creusement d’un tunnel à faible profondeur: 3D-
28 finite difference analysis of the interaction between concrete building and shallow
29 tunnelling. *Géotechnique* 54, 519–528.
- 30 Kasper, T., Meschke, G., 2004. A 3D finite element simulation model for TBM tunnelling
31 in soft ground. *Int. J. Numer. Anal. Methods Geomech.* 28, 1441–1460.
32 <https://doi.org/10.1002/nag.395>
- 33 Kavvadas, M., Litsas, D., Vazaios, I., Fortsakis, P., 2017. Development of a 3D finite
34 element model for shield EPB tunnelling. *Tunn. Undergr. Space Technol.* 65, 22–
35 34. <https://doi.org/10.1016/j.tust.2017.02.001>
- 36 Lambe, T., 1973. Predictions in soil engineering. *Géotechnique* 23, 151–202.
- 37 Lambrugh, A., Medina Rodríguez, L., Castellanza, R., 2012. Development and
38 validation of a 3D numerical model for TBM–EPB mechanised excavations.
39 *Comput. Geotech.* 40, 97–113. <https://doi.org/10.1016/j.compgeo.2011.10.004>
- 40 Litsas, D., Sitarenios, P., Kavvadas, M., 2018. Parametric investigation of tunnelling-
41 induced ground movement due to geometrical and operational TBM complexities.
42 *Ital. Geotech. J.* 51, 22–34. <https://doi.org/10.19199/2017.4.0557-1405.22>
- 43 Losacco, N., Burghignoli, A., Callisto, L., 2014. Uncoupled evaluation of the structural
44 damage induced by tunnelling. *Géotechnique* 64, 646–656.
45 <https://doi.org/10.1680/geot.13.P.213>
- 46 Losacco, N., Callisto, L., Burghignoli, A., 2016. Soil-structure interaction due to
47 tunnelling in soft ground, an equivalent solid approach. Presented at the

- 1 International Conference on Structural Analysis of Historical Constructions, CRC
2 Press, Leuven, Belgium, pp. 495–502.
- 3 Mair, R., Taylor, R., 1999. Theme lecture: Bored tunneling in the urban environment, in:
4 Proceedings of the Fourteenth International Conference on Soil Mechanics and
5 Foundation Engineering (Hamburg, 1997), Balkema. pp. 2353–2385.
- 6 Mair, R.J., Taylor, R., 1996. Geotechnical aspects of underground construction in soft
7 ground. Balkema.
- 8 Mašin, D., 2005. A hypoplastic constitutive model for clays. *Int. J. Numer. Anal. Methods*
9 *Geomech.* 29, 311–336. <https://doi.org/10.1002/nag.416>
- 10 Mayne, P.W., Kulhawy, F.H., 1982. K_0 -OCR Relationships in Soil. *J. Geotech. Eng. Div.*
11 108, 851–872.
- 12 Meschke, G., Nagel, F., Stascheit, J., 2011. Computational Simulation of Mechanized
13 Tunneling as Part of an Integrated Decision Support Platform. *Int. J. Geomech.*
14 11, 519–528. [https://doi.org/10.1061/\(ASCE\)GM.1943-5622.0000044](https://doi.org/10.1061/(ASCE)GM.1943-5622.0000044)
- 15 Migliazza, M., Chiorboli, M., Giani, G.P., 2009. Comparison of analytical method, 3D
16 finite element model with experimental subsidence measurements resulting from
17 the extension of the Milan underground. *Comput. Geotech.* 36, 113–124.
18 <https://doi.org/10.1016/j.compgeo.2008.03.005>
- 19 Moh, Z.C., Ju, D.H., Hwang, R.N., 1996. Ground movements around tunnels in soft
20 ground, in: Mair, R.J., Taylor, R.N. (Eds.), *Proceedings International Symposium*
21 *on Geotechnical Aspects of Underground Construction in Soft Ground*.
22 Rotterdam, The Netherlands: Balkema, London, UK, pp. 725–730.
- 23 Mroueh, H., Shahrour, I., 2008. A simplified 3D model for tunnel construction using
24 tunnel boring machines. *Tunn. Undergr. Space Technol.* 23, 38–45.
25 <https://doi.org/10.1016/j.tust.2006.11.008>
- 26 Negro, A., 1998. ‘General report: Design criteria for tunnels in metropolises, in: *Proc.*,
27 *World Tunnel Congress 1998 on Tunnels and Metropolises*. pp. 201–214.
- 28 Niemunis, A., Herle, I., 1997. Hypoplastic model for cohesionless soils with elastic strain
29 range. *Mech. Cohesive-Frict. Mater.* 2, 279–299.
- 30 Ochmański, M., Modoni, G., Bzówka, J., 2018. Automated numerical modelling for the
31 control of EPB technology. *Tunn. Undergr. Space Technol.* 75, 117–128.
32 <https://doi.org/10.1016/j.tust.2018.02.006>
- 33 Peck, R.B., 1969. Deep excavations and tunneling in soft ground, in: *Proceedings of the*
34 *Seventh International Conference on Soil Mechanics and Foundation*
35 *Engineering*. Mexico City, pp. 225–290.
- 36 Rampello, S., Callisto, L., Soccodato, F., Viggiani, G., 2012. Evaluating the effects of
37 tunnelling on historical buildings, in: *Geotechnical Aspects of Underground*
38 *Construction in Soft Ground*. CRC Press, pp. 47–62.
39 <https://doi.org/10.1201/b12748-6>
- 40 Roscoe, K., Burland, J., 1968. On the generalized stress-strain behaviour of wet clay.
- 41 Viggiani, G., Soccodato, F.M., 2004. Predicting tunnelling-induced displacements and
42 associated damage to structures. *Ital. Geotech. J.* 38, 11–25.
- 43 von Wolffersdorff, P.-A., 1996. A hypoplastic relation for granular materials with a
44 predefined limit state surface. *Mech. Cohesive-Frict. Mater.* 1, 251–271.
45 [https://doi.org/10.1002/\(SICI\)1099-1484\(199607\)1:3<251::AID-](https://doi.org/10.1002/(SICI)1099-1484(199607)1:3<251::AID-CFM13>3.0.CO;2-3)
46 [CFM13>3.0.CO;2-3](https://doi.org/10.1002/(SICI)1099-1484(199607)1:3<251::AID-CFM13>3.0.CO;2-3)

1 Wan, M.S.P., Standing, J.R., Potts, D.M., Burland, J.B., 2017. Measured short-term
2 subsurface ground displacements from EPBM tunnelling in London Clay.
3 *Géotechnique* 67, 748–779. <https://doi.org/10.1680/jgeot.SIP17.P.148>
4

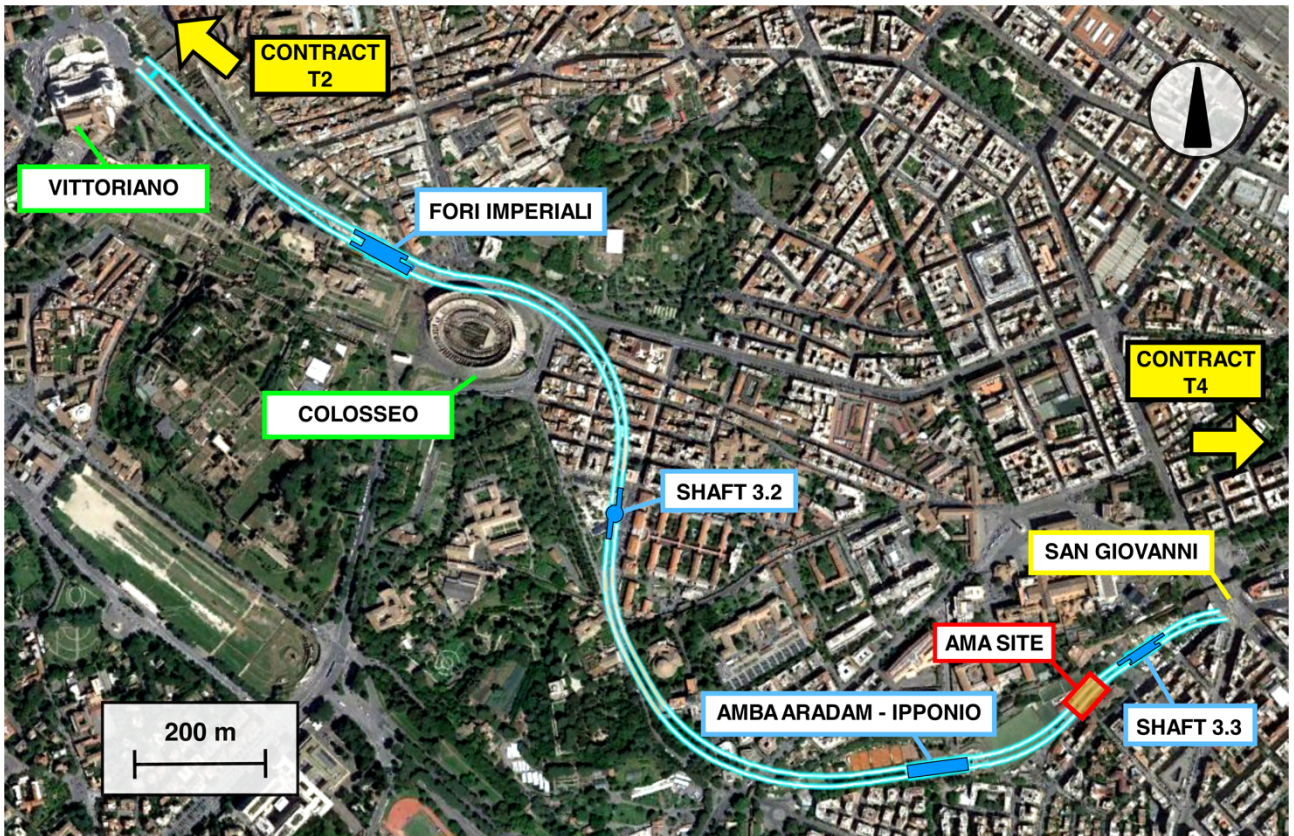


Fig. 1 - Aerial view of contract T3 of Line C of Rome underground, location of instrumented site. Modified from Google Maps 2018)

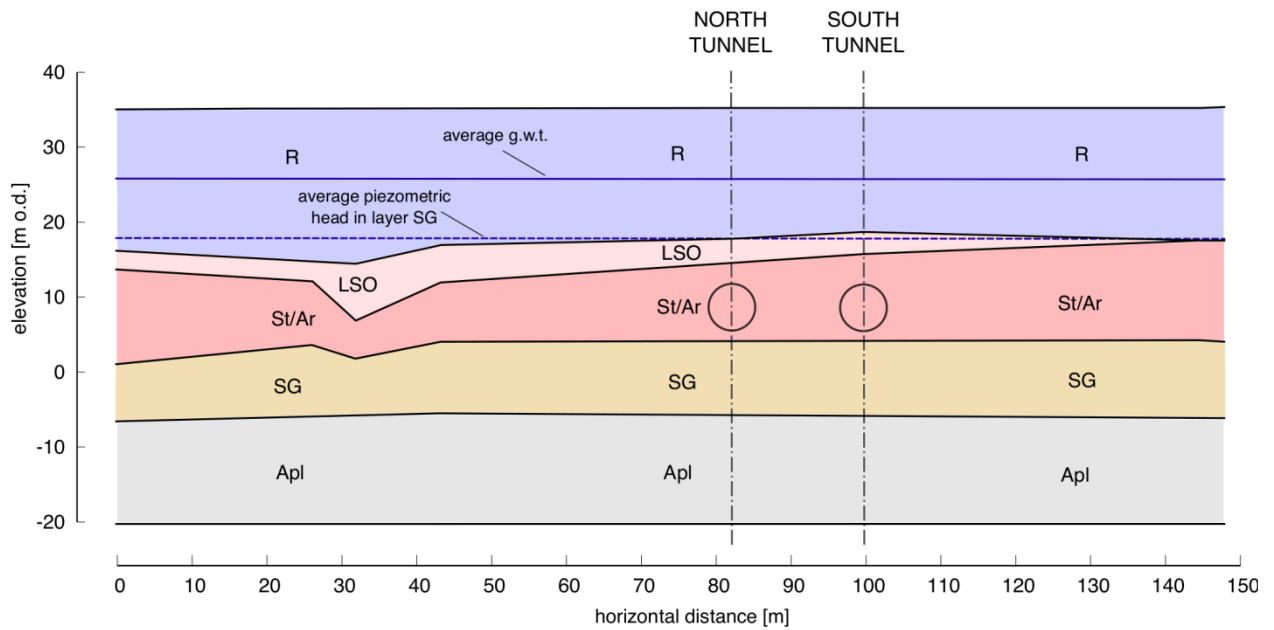


Fig. 2 - Geological section at AMA site

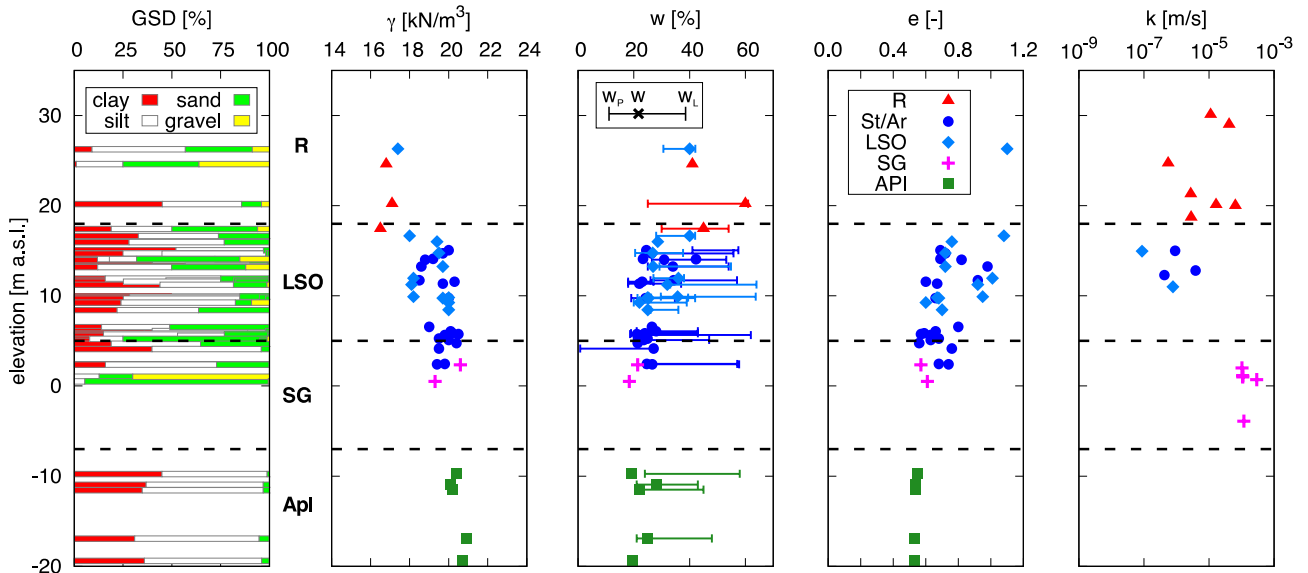


Fig. 3 – Main physical properties at AMA site: GSD, Grain Size Distribution; γ , unit weight; w_L , liquid limit; w , natural water content; w_p , plastic limit; e , voids ratio k , permeability

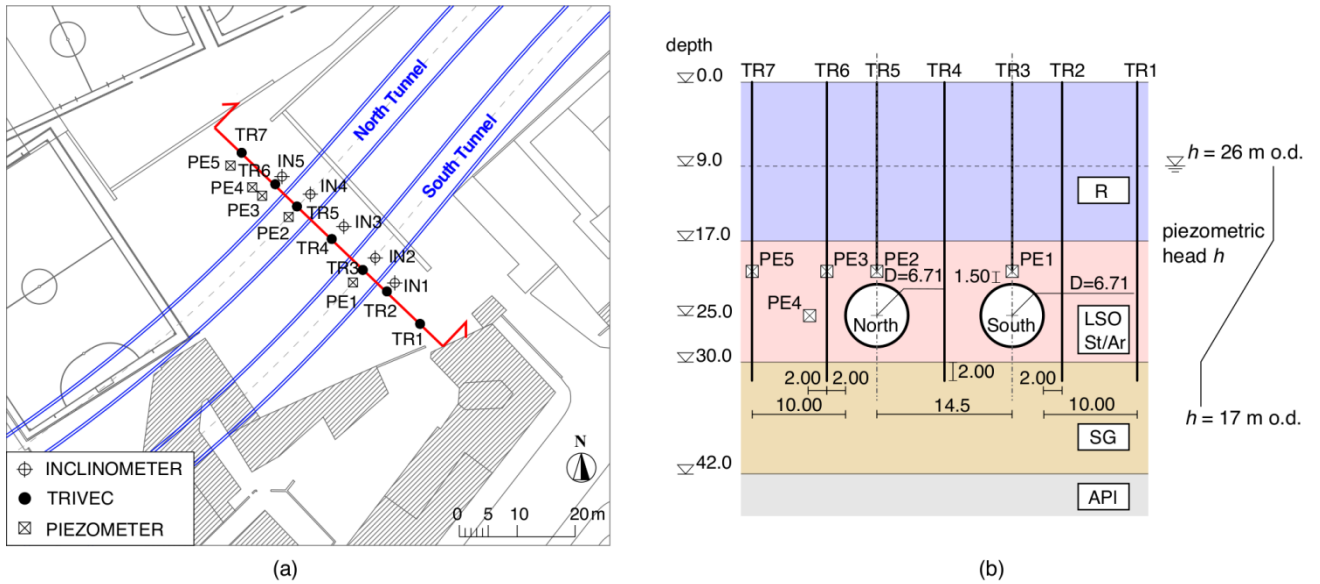


Fig. 4 – AMA site: plan view (a) and control section (b)

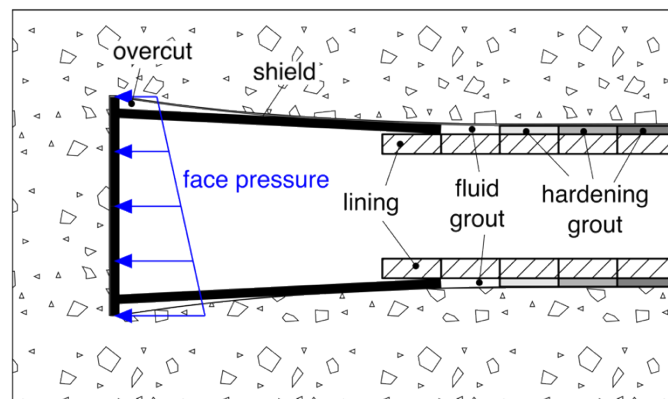


Fig. 5 – Features of mechanised tunnelling introduced in numerical simulation (not to scale)

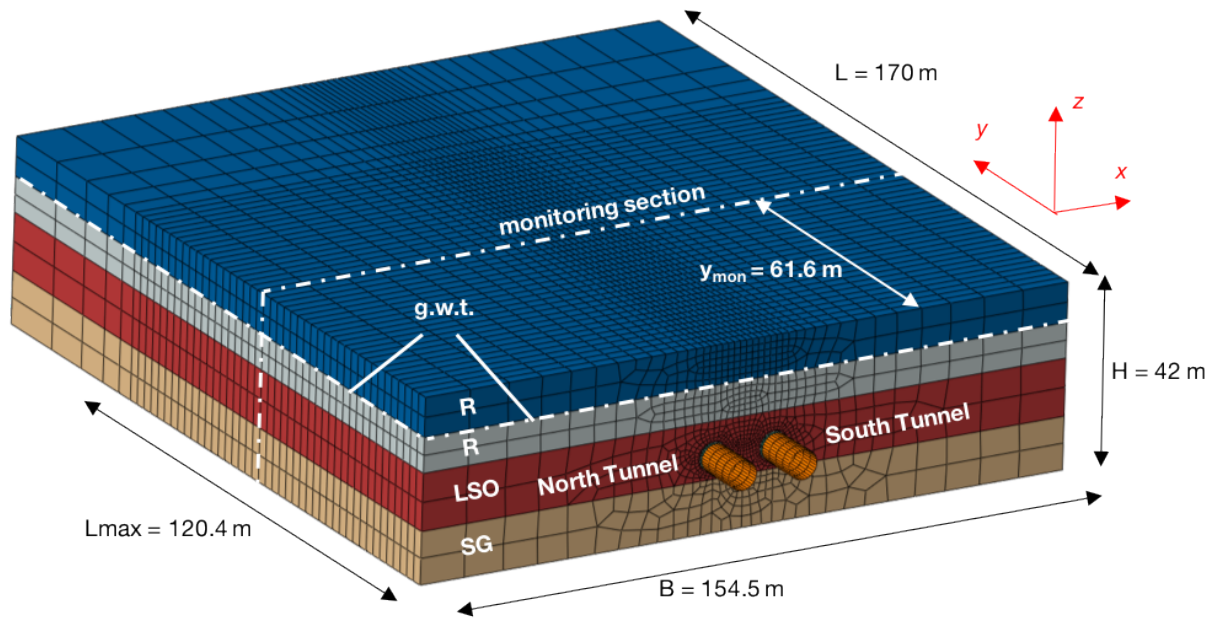


Fig. 6 - FE mesh

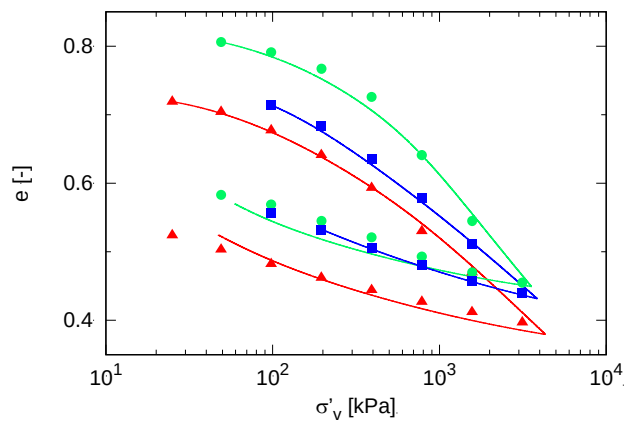


Fig. 7 - Calibration of parameters N , λ^* and k^* from oedometer tests on LSO samples

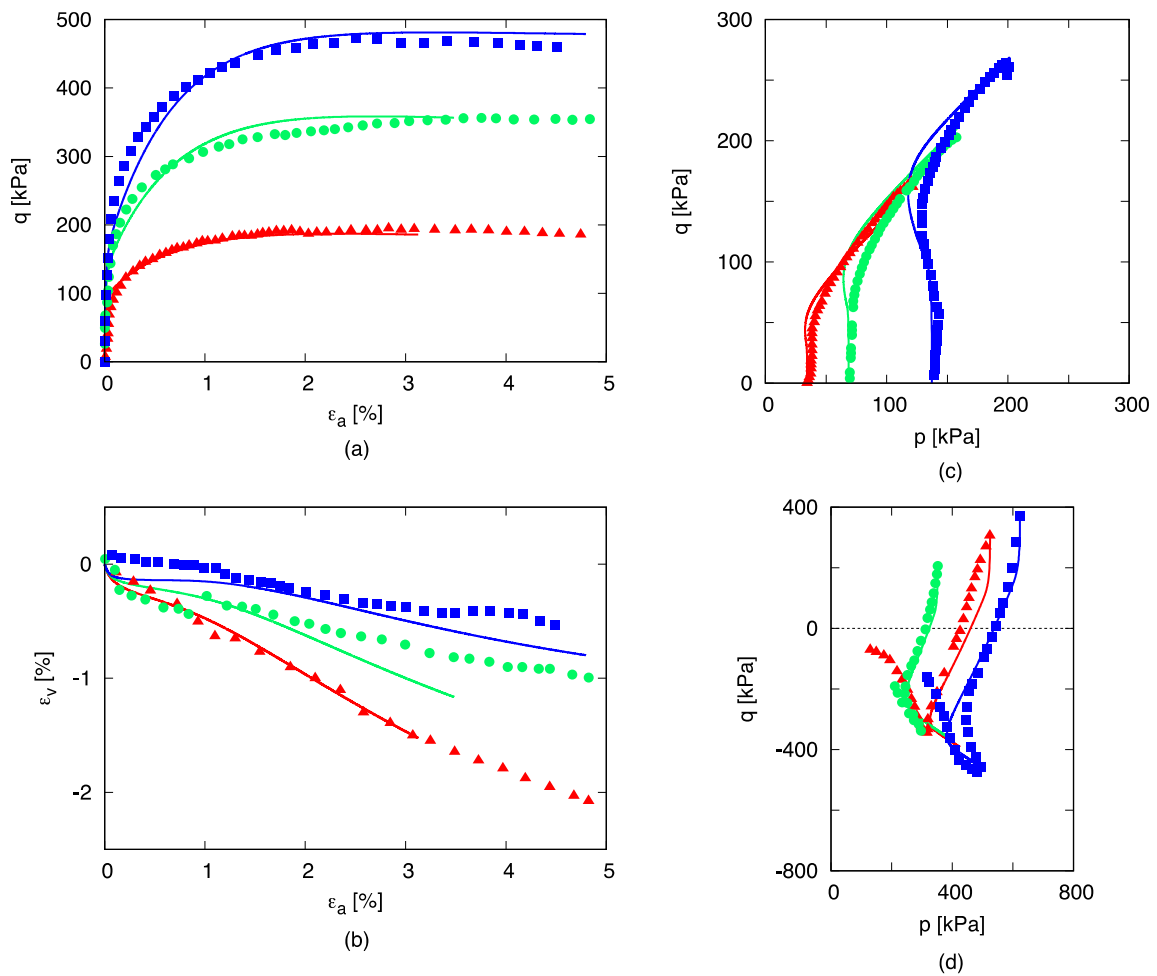


Fig. 8 - Calibration of hypoplastic model for clays from triaxial tests on LSO samples: CID (a, b); CIU (c); CK₀U (d)

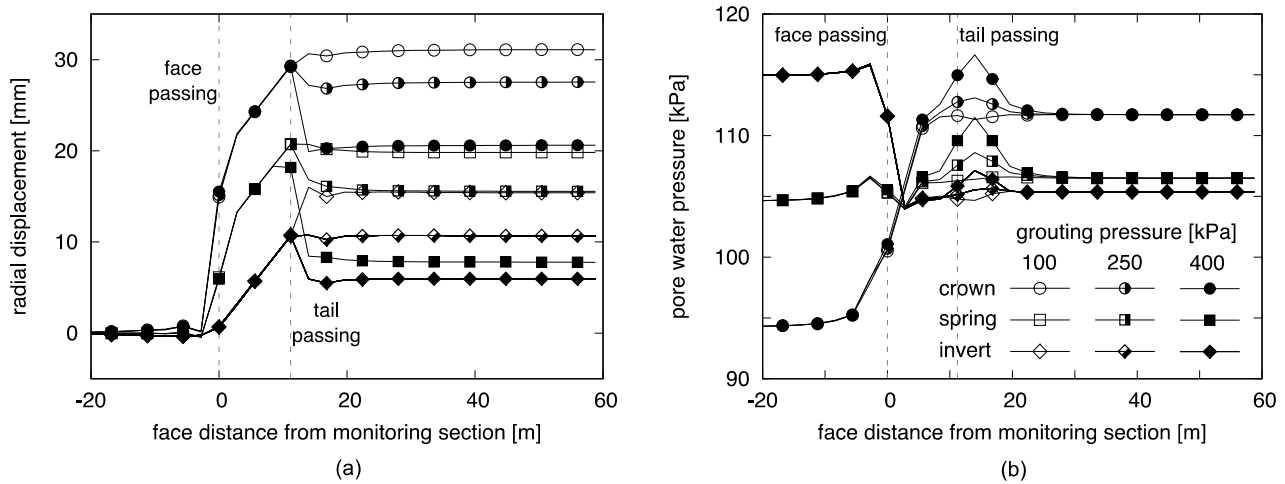


Fig. 9 - Preliminary analyses: (a) radial displacements (positive towards tunnel axis); (b) pore water pressure

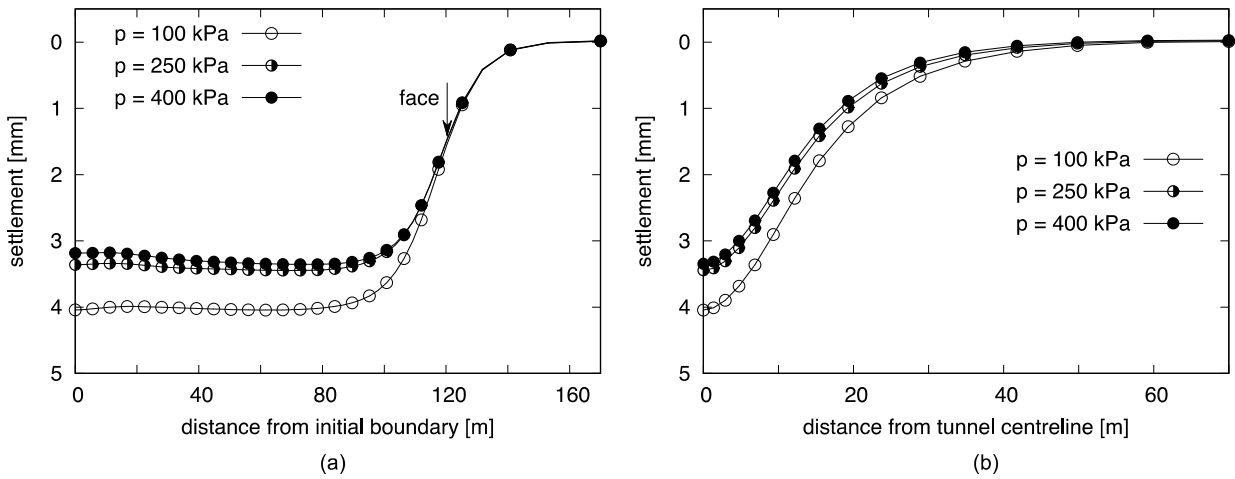


Fig. 10 - Preliminary analyses: longitudinal (a) and transverse (b) settlement troughs

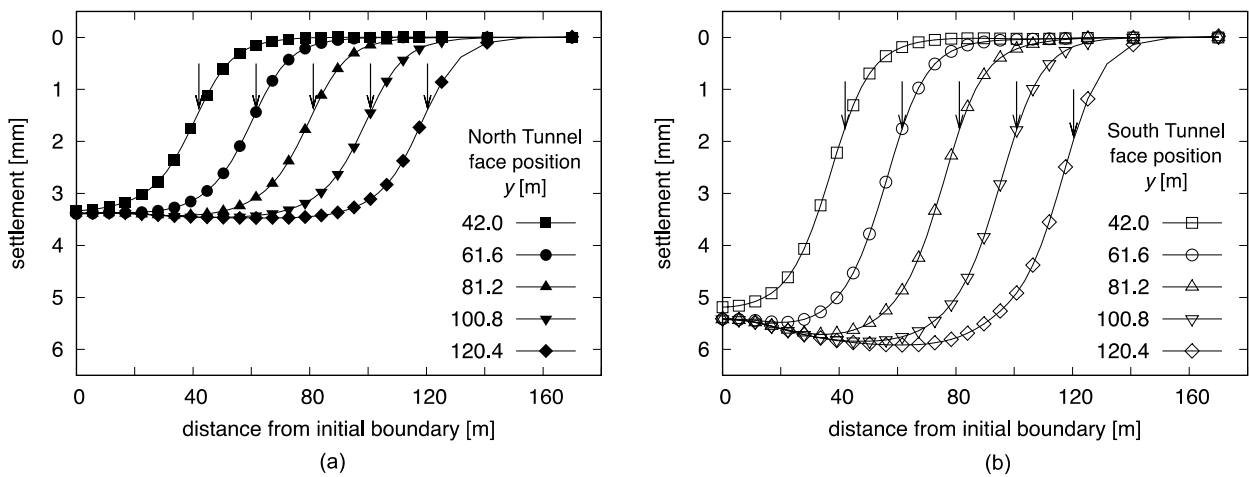


Fig. 11 - Class A predictions, longitudinal settlement trough: (a) North (b) South Tunnel (arrows indicate position of tunnel face)

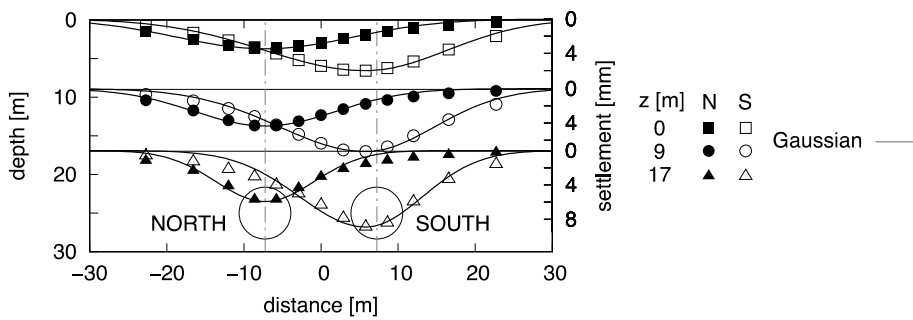


Fig. 12 - Class A predictions: transverse settlement troughs at various depths

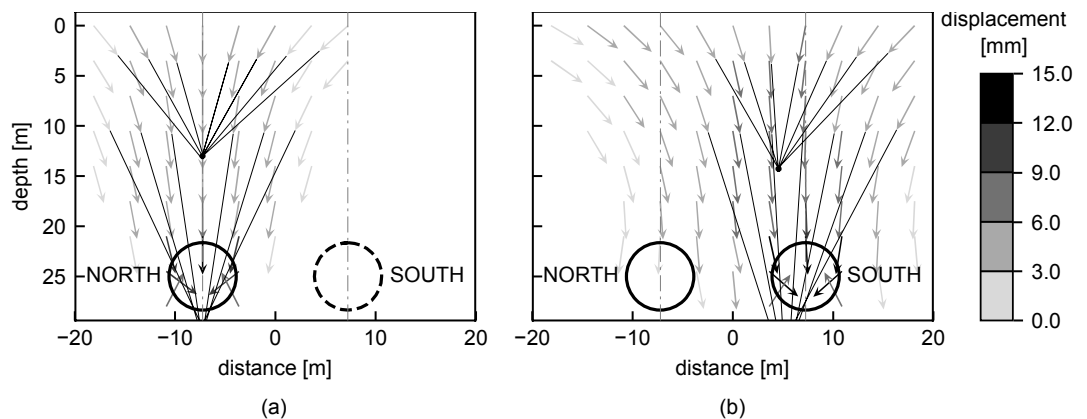


Figure 13 - Class A predictions, incremental displacement vectors: (a) North Tunnel and (b) South Tunnel

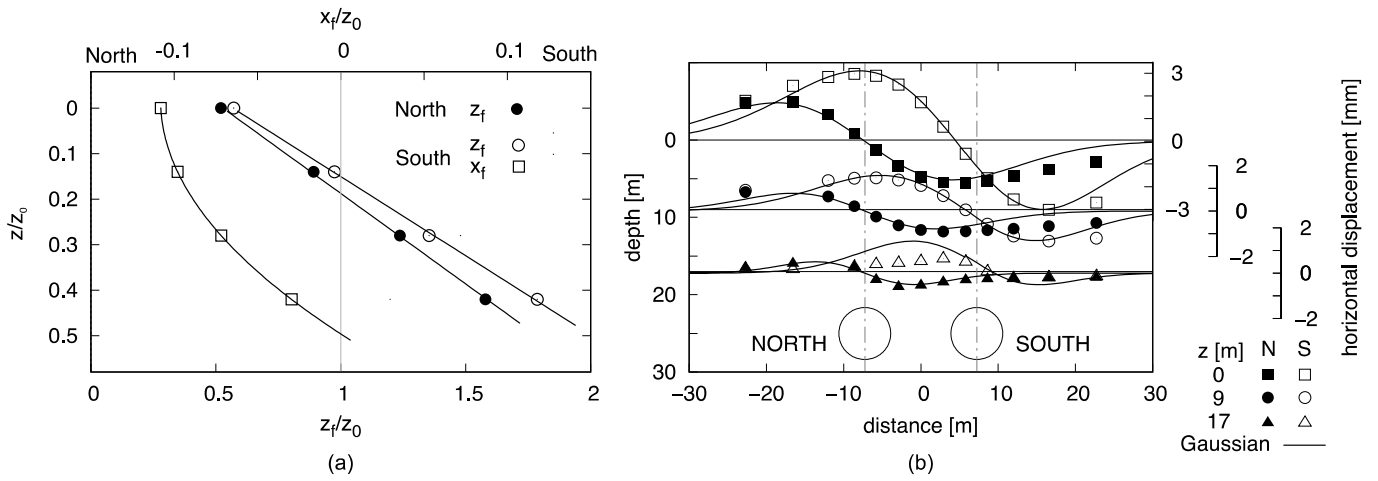


Fig. 14 – Class A predictions: (a) incremental displacements foci and (b) transverse horizontal displacements at various depths

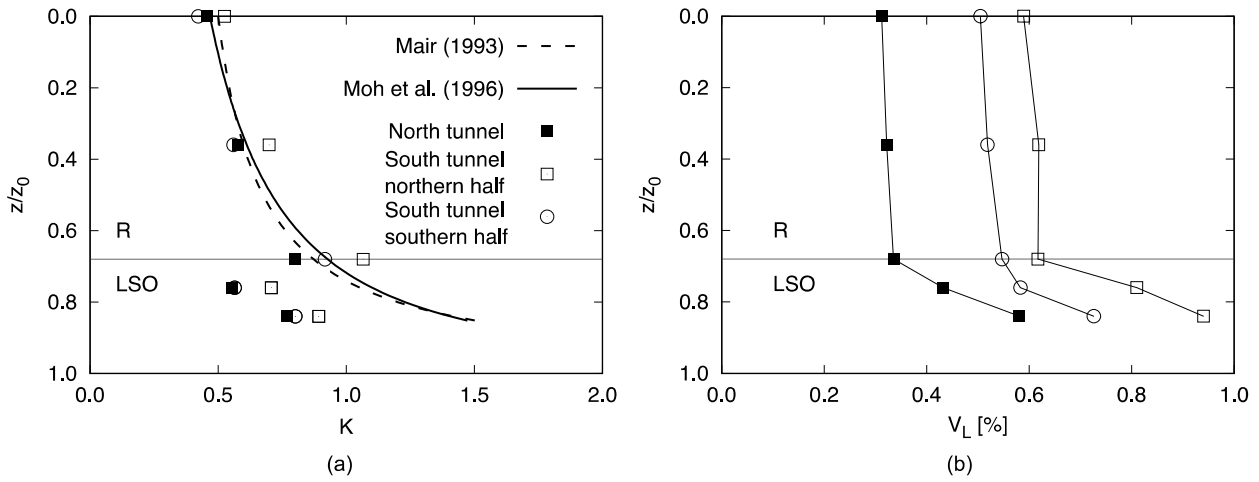
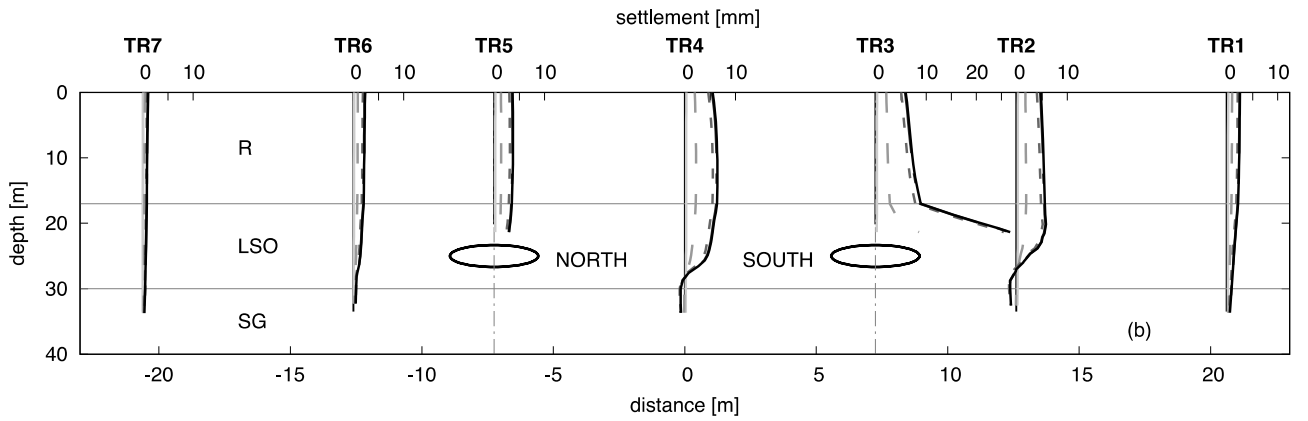
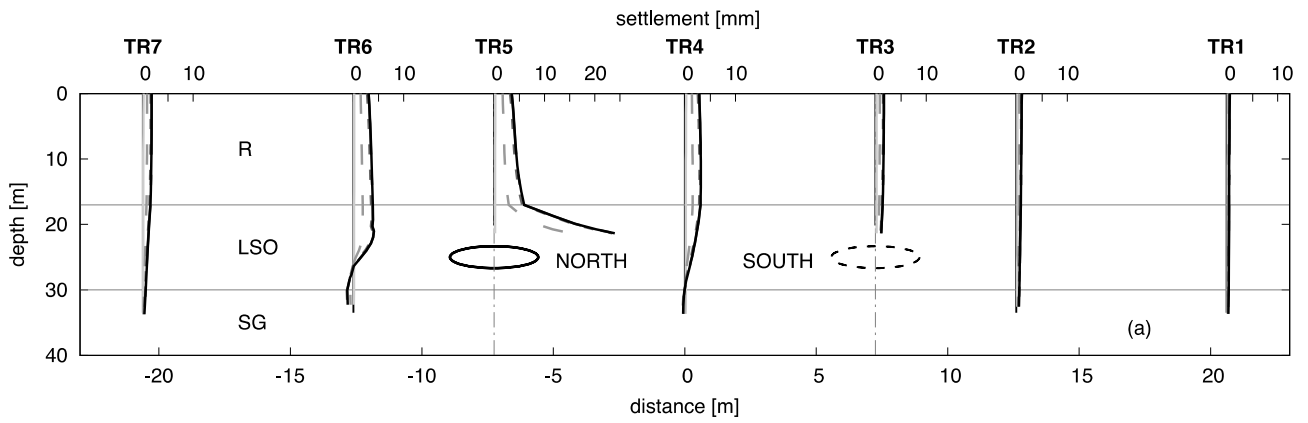
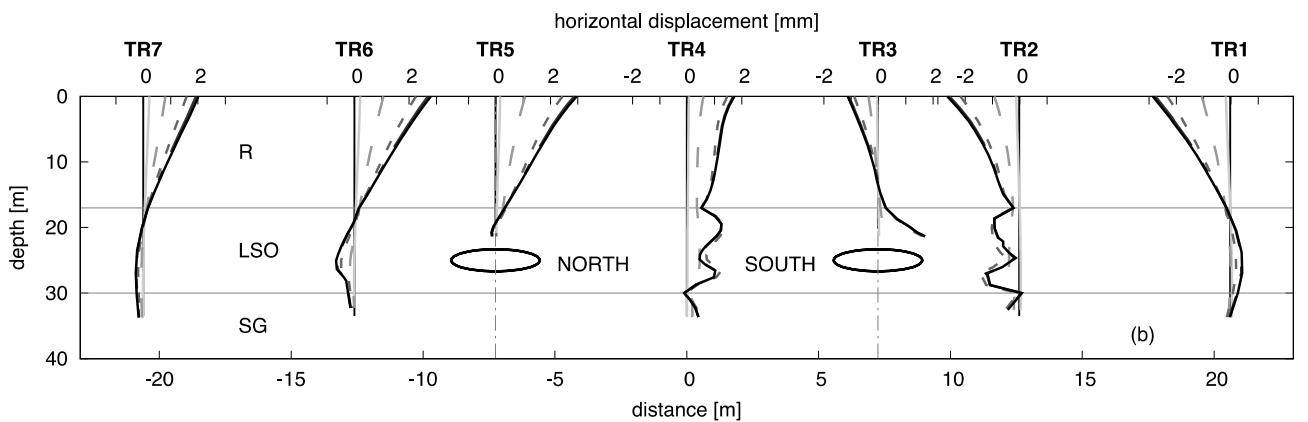
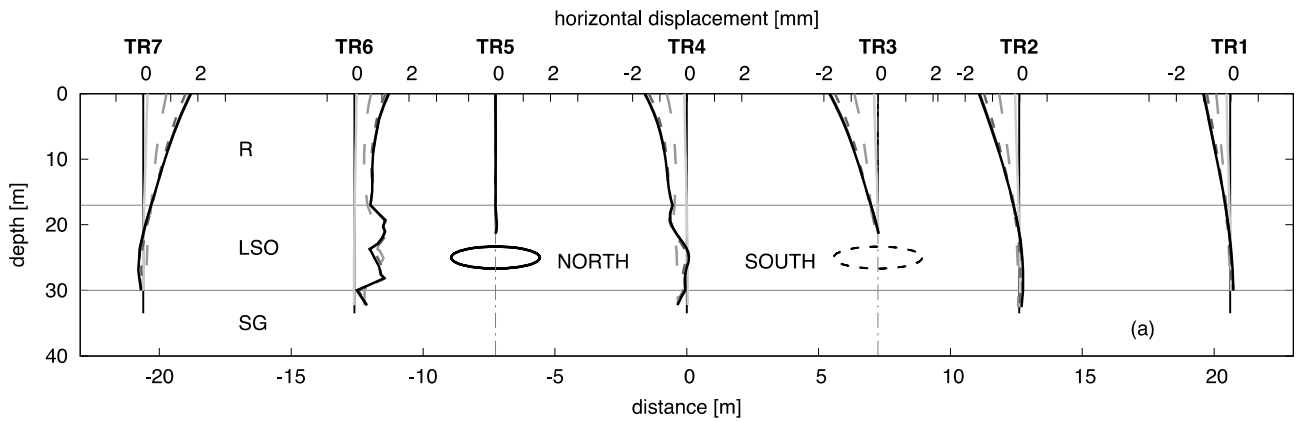


Fig. 15 – Class A predictions: profiles of (a) K and (b) volume loss with depth



tunnel face distance from monitoring section [m]
 -19.6 ——— 0.0 - - - 19.6 - - - - 39.2 - - - - 58.8 ———
 Fig. 16 - Class A predictions: profiles of incremental settlements for Trivecs: (a) North Tunnel, (b) South Tunnel



tunnel face distance from monitoring section [m]
 -19.6 ——— 0.0 - - - 19.6 - - - - 39.2 - - - - 58.8 ———
 Fig. 17 - Class A predictions: profiles of incremental horizontal displacements for Trivecs: (a) North Tunnel, (b) South Tunnel

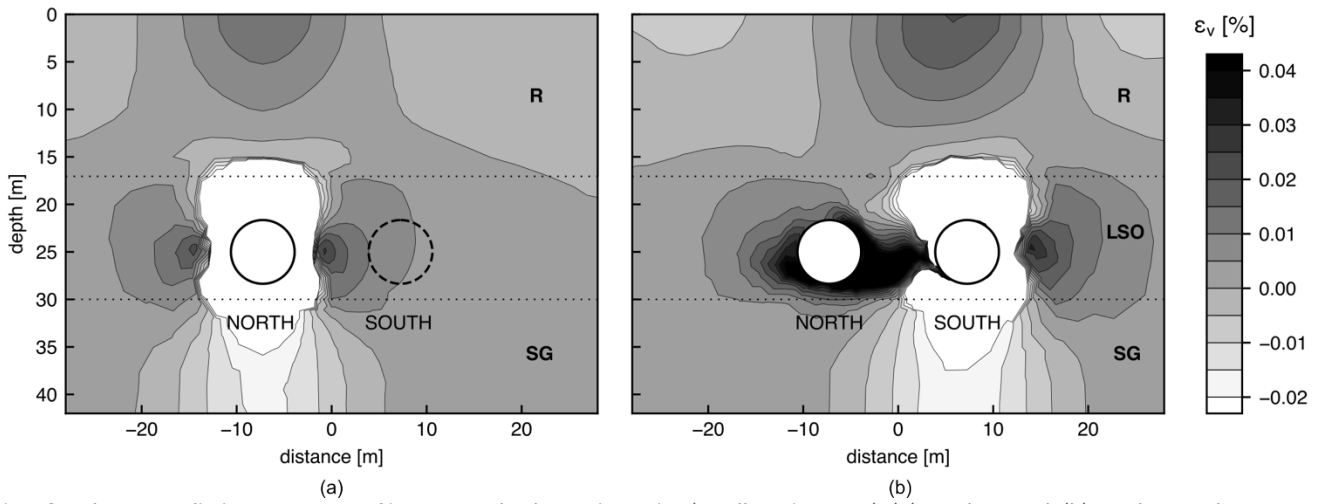


Fig. 18 – Class A predictions: contours of incremental volumetric strains (small strain range): (a) North Tunnel, (b) South Tunnel

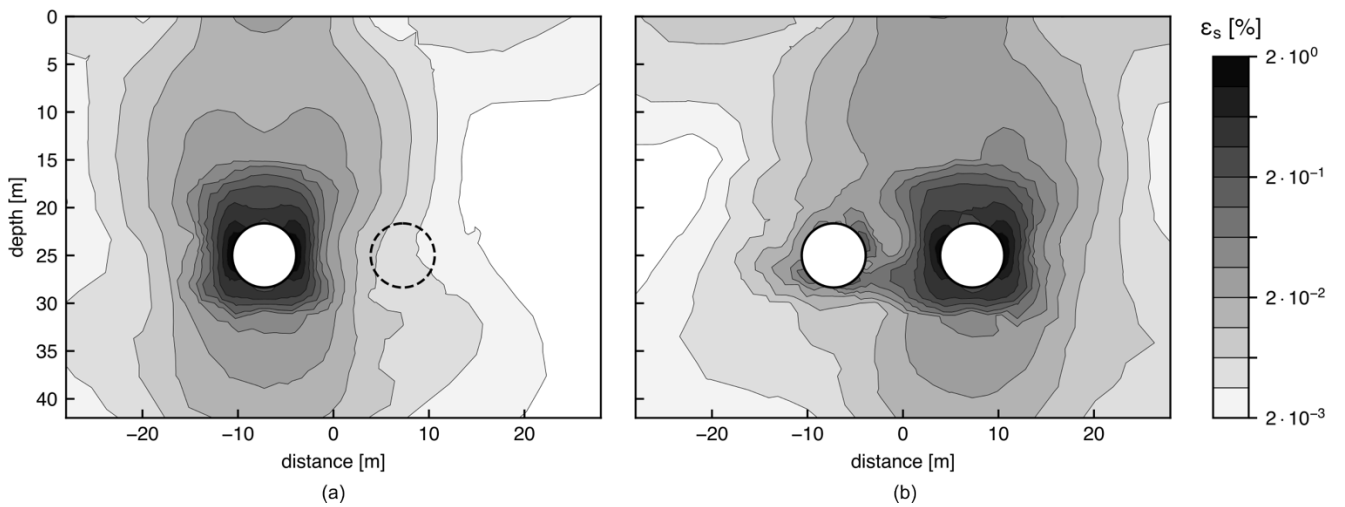


Fig. 19 – Class A predictions: contours of incremental deviatoric strains (log scale): (a) North Tunnel, (b) South Tunnel

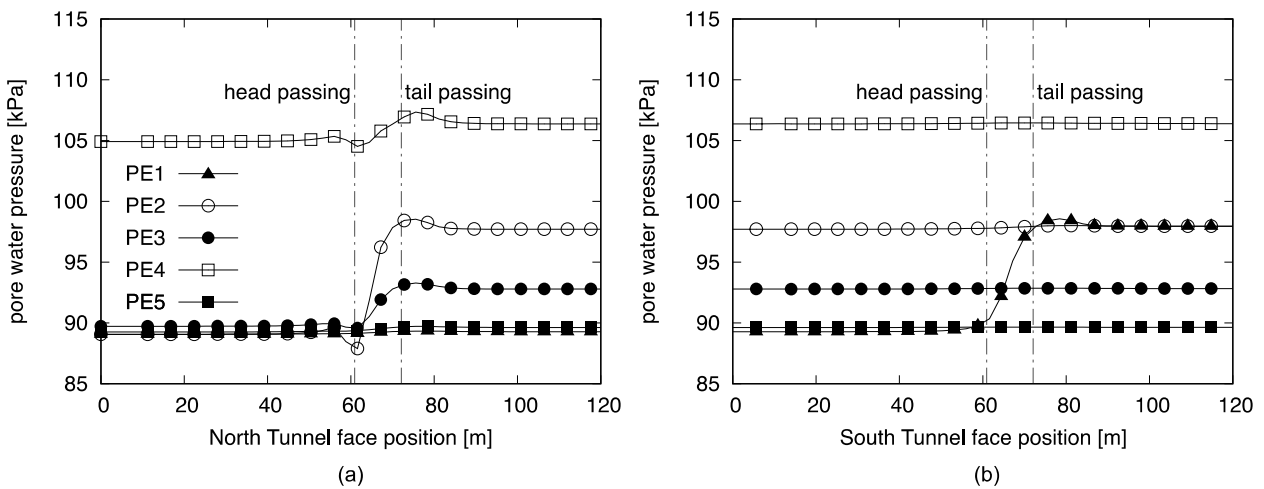


Fig. 20 – Class A predictions: pore water pressure for piezometers installed at monitoring section: (a) North Tunnel; (b) South Tunnel

Table 1: layer R - material constants for hypoplastic model for granular material and physical properties

h_s	n	e_{10}	e_{∞}	e_{d0}	ϕ'_c [°]	a	β	m_R	m_T	R	β_r	χ	γ [kN/m ³]	k [m/s]	K_o
3.4E+6	0.24	1.1	0.9	0.525	34	0.19	1.5	13.5	2.0	1.E-4	0.5	6.0	17.0	1.E-5	0.441

Table 2: layer LSO - material constants for hypoplastic model for clay and physical properties

ϕ'_c [°]	N	λ^*	κ^*	ν	Ag	n_g	m_{RAT}	R	β_r	χ	γ [kN/m ³]	k [m/s]	K_o
33	0.942	.075	0.012	0.2	18384.0	0.427	0.5	1.E-4	0.4	1.3	19.5	1.E-6	0.525

Table 3: layer SG - material constants for linear elastic – perfectly plastic model and physical properties

ϕ'_c [°]	c' [kPa]	E' [MPa]	ν'	γ [kN/m ³]	k [m/s]	K_o
45	0.0	316	0.2	20.0	1E-4	0.293